Check for updates

Small Methods

small methods
www.small-methods.com

RESEARCH ARTICLE

Unlocking Limited Na-Ion Transport Channel in $Na_2Fe_2(SO_4)_3$ for Ultrafast Na-Ion Transport

Yalan Gu[1] | Ye Hong[2] | Jiaojing Shao[3] | Jiwei Hou[4] | Zilong Tang[5] | Qinfen Gu[6] | Yuping Wu[7,8] | Linfeng Hu[1,8]

[1]School of Materials Science and Engineering, Southeast University, Nanjing, P. R. China | [2]Industrial Training Center, Guangdong Polytechnic Normal University, Guangzhou, P. R. China | [3]School of Materials and Metallurgy, Guizhou University, Guiyang, P. R. China | [4]Department of Physics, School of Physical and Mathematical Science, Nanjing Tech University, Nanjing, Jiangsu, P. R. China | [5]State Key Laboratory of New Ceramics and Fine Processing, School of Materials Science and Engineering, Tsinghua University, Beijing, P. R. China | [6]Australian Synchrotron, ANSTO, Clayton, VIC, Australia | [7]School of Energy and Environment, Southeast University, Nanjing, P. R. China | [8]Z Energy Storage Center, Southeast University, Nanjing, P. R. China

Correspondence: Linfeng Hu (linfenghu@seu.edu.cn)

Received: 6 March 2026 | **Revised:** 18 April 2026 | **Accepted:** 29 April 2026

Keywords: alluaudite-type $Na_2Fe_2(SO_4)_3$ | fe-site substitution | ion diffusion kinetics | Na—O bond elongation | sodium-ion batteries

ABSTRACT

Alluaudite-type $Na_2Fe_2(SO_4)_3$ has emerged as a promising cathode material for sodium-ion batteries (SIBs) owing to its high operating voltage (~3.80 V vs. Na^+/Na). Nevertheless, its practical rate performance is hindered by the sluggish Na^+ transport. In this work, we realized the synergetic elongation of Na_2—O/Na_3—O bonds to widen the sodium ion transport channels by Ca, Mn, Cu co-doping. Specifically, Ca doping induced the elongation of the Na_2—O_5 and Na_2—O_5' bonds; Mn doping resulted in the extension of the Na_2—O_1 bond; and Cu doping led to the increase in the Na_3—O_4 and Na_3—O_4' bond lengths. Strikingly, the optimized $Na_2Fe_{1.9}Ca_{0.03}Mn_{0.035}Cu_{0.035}(SO_4)_3$ exhibits ultrafast sodium ion diffusion coefficient in the range of 10^{-10} to 10^{-8} $cm^2 \cdot s^{-1}$, which is the highest one among the $Na_2Fe_2(SO_4)_3$ cathode up to date. Density functional theory (DFT) calculations confirm that co-doping can reduce the Na^+ migration barrier. The sodium ion half-cell using this co-doped cathode delivers excellent rate capability (97, 80, and 69 $mAh \cdot g^{-1}$ at 0.1, 1.0, and 3.0 $A \cdot g^{-1}$, respectively) and excellent cycling stability of 5000 cycles. Our work provides new insights on the structural evolution of Na_2—O/Na_3—O bonds by multiple metallic cations substitution of Fe-site in $Na_2Fe_2(SO_4)_3$ to realize high sodium ion transport kinetics.

1 | Introduction

Sodium-ion batteries (SIBs) are considered promising candidates for large-scale energy storage devices due to their low cost and excellent stability [1–5]. The mainstream cathode materials for SIBs primarily include Prussian blue analogs (PBAs) with open three-dimensional frameworks, layered metal oxides with tunable interlayer spacing, and polyanionic-type compounds. Among them, PBAs feature a robust cubic framework with large ion channels, enabling fast Na^+ insertion/extraction, while layered oxides deliver high specific capacity [6–8]. In particular, Fe-based sodium iron sulfates have gained significant attention as promising cathode materials for SIBs owing to the nontoxicity and abundance of Fe [9–11]. As first reported by Yamada in 2014 [12–14], the alluaudite-typed iron-based sodium sulfate, $Na_2Fe_2(SO_4)_3$, shows Na^+ storage behavior with a high operating voltage (~ 3.80 V vs. Na^+/Na) and a competitive theoretical capacity (120 $mAh \cdot g^{-1}$) [15, 16]. The $Na_2Fe_2(SO_4)_3$ crystal is composed of the corner-sharing linkage of [FeO_6] octahedra and [SO_4] tetrahedra (Scheme 1), and its Na^+ storage ability originates from an open framework with tunnel-type Na^+ migration channels along the *c*-axis [12–14, 17, 18] Theoretically, the migration of Na

© 2026 Wiley-VCH GmbH

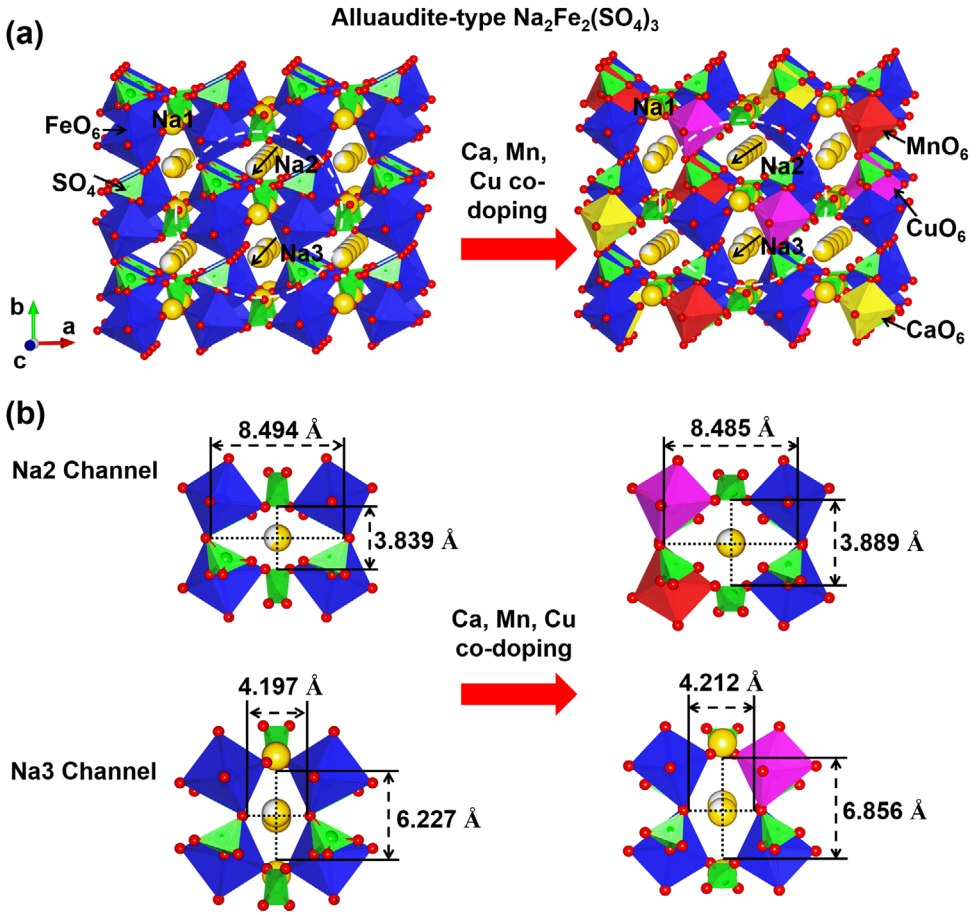

SCHEME 1 | (a) Crystal structure of alluaudite-typed $Na_2Fe_2(SO_4)_3$ and multiple cations co-doped $Na_2Fe_2(SO_4)_3$ to illustrate the one-dimensional Na^+ migration channel along the *c*-axis. (b) Sizes of the Na_2 and Na_3 channels of NFS and co-doped-NFS. In the figure, the dark blue octahedra represent FeO_6, the yellow octahedra represent CaO_6, the red octahedra represent MnO_6, the purplish-red octahedra represent CuO_6, the green tetrahedra represent SO_4, the yellow spheres represent Na, and the red spheres represent O. Within the alluaudite-type $Na_2Fe_2(SO_4)_3$ framework (general formula $AA'BM_2(XO_4)_3$, $A = Na_2$, $A' = Na_3$, $B = Na_1$, $M =$ Fe, and $X =$ S), three distinct sodium ion sites are present: the Na1 site is fully occupied albeit with no open channels for migration, while the Na2 and Na3 sites are partially occupied with tunnels for one-dimensional migration along the *c*-axis. Na_2 is coordinated to three oxygen atoms via Na_2—O_1, Na_2—O_5, and Na_2—O_5' bonds, while Na3 is coordinated to two oxygen atoms through Na_3—O_4 and Na_3—O_4' bonds [12–14, 17, 18, 32].

ions within iron sulfate crystals depends on the gaps between the polyhedral (e.g., [FeO_6] octahedra and [SO_4] tetrahedra) [19, 20]. During migration, Na^+ is hindered by electrostatic repulsion from adjacent cations and electrostatic attraction induced by highly electronegative SO_4^{2-}. These effects lead to sluggish Na^+ transport kinetics and unsatisfactory electrochemical performance in sodium-ion full batteries [21–23]. Realizing ultrafast Na^+ transport kinetics in alluaudite-type iron-based sulfates remains a great challenge due to their structural limitations [24, 25].

Recent progress demonstrates that crystal structure modulation of sodium iron sulfate is an effective pathway to enhance its electrochemical performance [19, 26–28]. Typically, Cao et al. [26] reported a phosphate radical (PO_4^{3-}) substitution in $Na_2Fe_2(SO_4)_3$ to alleviate the Coulombic repulsion between Fe ions and Fe ions. The introduction of PO_4^{3-} can enhance Na-ion/electron transport kinetics, minimize volume change and ensure a stable framework. Chen et al. [19] recently developed a Mg-substituted sodium iron sulfate using a cation-inspired strategy. They reported that the substituted [MgO_6] octahedra feature stronger covalent bonding interactions and provide wider gap channels for Na^+ transport within the crystals. Based on these pioneering works, we consider whether multiple cations could be simultaneously doped into the $Na_2Fe_2(SO_4)_3$ crystal to substitute Fe sites and achieve a synergetic modulation effect. However, up to date, there are no fundamental studies on multi-cation substitution in sodium iron sulfate, and a deep understanding of the synergetic mechanism is still lacking to effectively address the sluggish Na^+ transport kinetics for this promising SIBs cathode.

Our group previously developed a series of structural modulation on phosphate-based polyanion compounds (such as $VOPO_4{\cdot}2H_2O$, $Na_4VMn(PO_4)_3$) for high-performance aqueous energy storage [29–31]. Based on this, herein we carried out a systematic study on the structural modulation of $Na_2Fe_2(SO_4)_3$ through multiple cations substitution strategy to significantly expand Na^+ ion diffusion pathways. After a systematical study on the effect of Ca, Mn, Cu, Mg, Al, Ti, V, Co, Ni, Zn single-element doping, the optimal Ca, Mn, Cu species were successfully introduced into the $Na_2Fe_2(SO_4)_3$ host to form a uniform

23669608, 0, Downloaded from https://onlinelibrary.wiley.com/doi/10.1002/smtd.70703 by Hu linfeng - Southeast University , Wiley Online Library on [11/05/2026]. See the Terms and Conditions (https://onlinelibrary.wiley.com/terms-and-conditions) on Wiley Online Library for rules of use; OA articles are governed by the applicable Creative Commons License

$Na_2Fe_{1.9}Ca_{0.03}Mn_{0.035}Cu_{0.035}(SO_4)_3$ solid solution. The co-doping of these three cations induced distinct variations in the lengths of the Na—O bonds. Specifically, the bond length increments (Δ) for co-doped-NFS are $\Delta Na_2—O_1$ = 0.0071 Å, $\Delta Na_2—O_5$ = 0.0056 Å, $\Delta Na_2—O_5'$ = 0.0054 Å, $\Delta Na_3—O_4$ = 0.0119 Å, and $\Delta Na_3—O_4'$ = 0.0203 Å (Scheme 1). The synergetic expansion of $Na_2—O_1$, $Na_2—O_5$, $Na_2—O_5'$, $Na_3—O_4$, and $Na_3—O_4'$ bond leads to a widening of Na^+ migration channels, thereby remarkably enhancing the Na^+ diffusion coefficients ranging from 10^{-10} to 10^{-8} $cm^2 \cdot s^{-1}$, which represent the highest values as-reported for sodium iron sulfate so far. DFT calculations further confirm the significant reductions in Na^+ migration energy barriers, the broadening of transport channels, enhanced density of states intensity near the Fermi level, and weakened Na^+ adsorption interaction with the material surface. Benefiting from the advance, the resulting $Na_2Fe_{1.9}Ca_{0.03}Mn_{0.035}Cu_{0.035}(SO_4)_3$ delivers a high energy density of 354.1 $Wh \cdot kg^{-1}$ at 0.1 $A \cdot g^{-1}$ and excellent rate capability (97, 80, and 69 $mAh \cdot g^{-1}$ at 0.1, 1.0, and 3.0 $A \cdot g^{-1}$, respectively). It also demonstrates excellent cycling stability over 5000 cycles. The as-assembled $Na_2Fe_{1.9}Ca_{0.03}Mn_{0.035}Cu_{0.035}(SO_4)_3$ //hard carbon full-cell delivers a high energy density of 248.0 $Wh \cdot kg^{-1}$ with a discharge plateau of 3.10 V and a specific capacity of 80 $mAh \cdot g^{-1}$ at 0.1 $A \cdot g^{-1}$.

2 | Results and Discussion

2.1 | Na—O Bond Evolution

In our work, Ca, Mn, Cu, Mg, Al, Ti, V, Co, Ni and Zn were selected as single-doping elements as their ionic radii are close to that of Fe^{2+} ions (Table S1). Highly crystalline $Na_2Fe_2(SO_4)_3$ (denoted as NFS) and a series of 5 atom % single-doped samples ($Na_2Fe_{1.9}M_{0.1}(SO_4)_3$, where M = Ca, Mn, Cu, Mg, Al, Ti, V, Co, Ni, Zn, denoted as M-NFS, etc.) were synthesized via a simple low-temperature calcination process of the precursors at 350°C under an atmosphere containing 5 vol% H_2 in Ar [33]. As shown in Figures S1–S3, all single-doped samples show powder x-ray diffraction (PXRD) patterns similar to those of NFS without any impurity peaks.

To elucidate the evolution of Na—O bonds length at the Na2 and Na3 sites and the crystal volume induced by various cations dopants in $Na_2Fe_2(SO_4)_3$, Rietveld refinement was performed on PXRD data of all of the aforementioned samples, which provides key insights into the local coordination environments of Na sites and their corresponding Na—O bond lengths. The weighted profile R-factors (R_{wp}) and goodness-of-fit (*GOF*) parameters for all refined samples fall within reasonable ranges, verifying the high reliability of the refinement results (Figures S1–S3 and Table S2). The refinement results reveal a remarkable change on Na—O bond length by Ca, Mn, Cu doping as follows (Figure 1, Table 1, Table S3): (1) Ca doping exerts the strongest effect in lengthening the $Na_2—O_5$ and $Na_2—O_5'$ bonds ($\Delta Na_2—O_5$: 0.0094 Å, $\Delta Na_2—O_5'$: 0.0061 Å); (2) Mn doping induces the most significant elongation of the $Na_2—O_1$ bond ($\Delta Na_2—O_1$: 0.0102 Å); (3) Cu doping leads to the largest increase in the bond lengths of $Na_3—O_4$ and $Na_3—O_4'$ ($\Delta Na_3—O_4$: 0.0143 Å, $\Delta Na_3—O_4'$: 0.0222 Å). Meanwhile, (Figure S4, Tables S4 and S5), the lattice parameter *b* and *c* of Mn-NFS increased owing to the elongation of $Na_2—O_1$ bond (Δb: 0.0045 Å, Δc: 0.0010 Å). Such results are also confirmed in the Ca-NFS and Cu-NFS samples, which exhibit elongated *a* and *c* lattice parameters (Ca-NFS: Δa: 0.0070 Å, Δc: 0.0040 Å; Cu-NFS: Δa: 0.0010 Å, Δc: 0.0010Å). However, we cannot observe such an obvious increase on Na_2—-O/Na_3—O bond length by other metallic cations doping. Even a shrinkage of the Na_2—O/Na_3—O bond was detected in some case of the introduction of Mg, Al, Ti, V, Co, Ni, Zn substitution (Figure 1a, Table 1, Table S3). Accordingly, the single-element doping results identify the Ca, Mn, Cu is the optimal dopant to enlarge the size of Na^+ transport channel.

Let us consider why this Ca, Mn, Cu doping results in such a remarkable increase on Na—O bond length. Since the ionic radii of Ca^{2+} and Mn^{2+} ion are larger than that of Fe^{2+} ion (Table S1), their incorporation into the $Na_2Fe_2(SO_4)_3$ lattice by occupying Fe sites may serve to expand the crystal structure. This doping behavior may directly expand the local coordination environment of the lattice, which induces an increase in unit cell volume and the elongation of Na—O bond lengths [34–36]. In the case of Cu^{2+} ion, which possesses higher electronegativity than Fe^{2+} (Table S1), its stronger electron-withdrawing ability may enhance the attraction toward coordinated oxygen atoms, thereby further triggering the compensatory elongation of the Na—O bonds surrounding the [CuO_6] octahedra [37, 38]. For other ions (e.g., Mg^{2+}, Ni^{2+}, Al^{3+}, Ti^{4+}, V^{3+}, Co^{2+} and Ni^{2+} ions), either the ion radii or electronegativities are lower than those of Fe^{2+}, further restricting their ability to stretch these bonds. Thus, the ion radii and electronegativities of the as-doped metallic cations play a crucial role in the Na—O bond length regulation in alluaudite-typed $Na_2Fe_2(SO_4)_3$.

2.2 | The Co-Doping of Ca, Mn, Cu

Guided by the conclusions from the single-element doping result, we further designed a Ca, Mn, Cu co-doped sample (denoted as co-doped-NFS) using the same calcination method. As shown in Figure 2a, co-doped-NFS sample also crystallizes in the same monoclinic system with the *C2/c* space group as pristine sample. All of the diffraction peaks that can be well indexed to the alluaudite phase (JCPDS No. 04-026-2145) without any impurity peaks Furthermore, scanning electron microscopy (SEM) observation indicates that co-doped-NFS mainly exhibits a particle-like morphology, similar to that observed in pristine NFS and the single-doped samples (Figure 2b; Figures S5–S7). N_2 adsorption-desorption measurement indicates a slight increase of specific surface area from pristine 6.40 to 9.63 $m^2 \cdot g^{-1}$ after co-doping (Figure S8). Transmission electron microscopy (TEM) image in Figure S9 indicates the size of the particle ranges in 1–3 μm (Supporting Information). High-resolution TEM (HRTEM) images of the pristine NFS exhibits clear lattice fringes, with interplanar spacings of 2.48 and 2.87 Å corresponding to the (112) and (002) planes, respectively. In contrast, the (112) and (002) interplanar spacings of the co-doped-NFS sample increase to 2.53 and 2.93 Å, respectively, and the expansion of the interplanar spacings confirms that the co-doping strategy successfully induces lattice expansion. Energy-dispersive x-ray spectroscopy (EDS) mapping (Figure 2c; Figure S10) demonstrates uniform distribution of Na, S, O, Fe, Ca, Mn, and Cu elements in co-doped-NFS. X-ray photoelectron spectroscopy (XPS) was employed to characterize the valence state of Fe and further verify that Ca, Mn, and

23669608, 0, Downloaded from https://onlinelibrary.wiley.com/doi/10.1002/smtd.70703 by Hu Inreng - Southeast University , Wiley Online Library on [11/05/2026]. See the Terms and Conditions (https://onlinelibrary.wiley.com/terms-and-conditions) on Wiley Online Library for rules of use; OA articles are governed by the applicable Creative Commons License

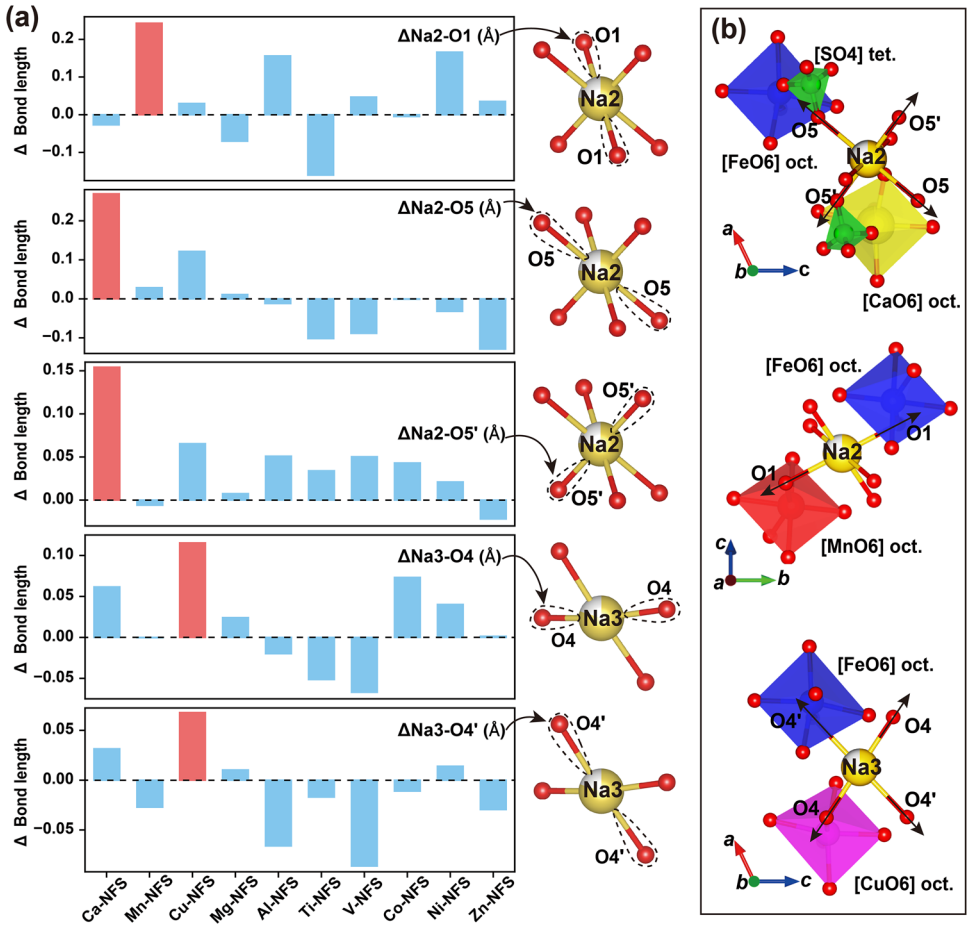

FIGURE 1 | (a) The discrepancy (Δ bond length) of Na2-O/Na3-O bond length in alluaudite-typed $Na_2Fe_2(SO_4)_3$ by Ca—, Mn—, Cu—, Mg—, Al—, Ti—, V—, Co—, Ni—, and Zn doping. (b) Schematic illustration of the Na—O bond coordination environment after Ca, Mn, Cu doping, respectively.

TABLE 1 | The discrepancy in Na_2—O_1, Na_2—O_5, Na_2—O_5' Na_3—O_4, and Na_3—O_4' bond lengths between pristine NFS and 5 atom % single-doped samples (Ca—, Mn—, Cu—, Mg—, Al—, Ti—, V—, Co—, Ni—, Zn-NFS) obtained from PXRD Rietveld refinement. ($Na_2Fe_{1.9}M_{0.1}(SO_4)_3$, where M = Ca, Mn, Cu, Mg, Al, Ti, V, Co, Ni, and Zn).

Sample	ΔNa_2—O_1 (Å)	ΔNa_2—O_5 (Å)	ΔNa_2—O_5' (Å)	ΔNa_3—O_4 (Å)	ΔNa_3—O_4' (Å)
Ca-NFS	0.0036	0.0094	0.0061	0.0027	0.0073
Mn-NFS	0.0102	0.0012	0.0014	0.0052	0.0083
Cu-NFS	−0.0019	0.0027	0.0045	0.0143	0.0222
Mg-NFS	−0.0055	−0.0141	−7E-4	−0.0034	−0.0065
Al-NFS	−0.0077	−0.0142	−0.0031	−0.0100	−0.0137
Ti-NFS	−0.0092	−0.0165	−5E-4	−0.0121	−0.0203
V-NFS	−0.0091	−0.0172	0.0000	−0.0129	−0.0097
Co-NFS	−0.0020	−0.0132	2E-4	0.0063	0.0080
Ni-NFS	−0.0068	−0.0162	2E-4	0.0091	0.0073
Zn-NFS	−0.0051	−0.0108	−0.0011	−0.0039	−0.0037

Cu dopants were successfully incorporated into the alluaudite-type $Na_2Fe_2(SO_4)_3$ lattice (Figure S11). The high-resolution Fe 2p spectrum of the co-doped sample shows distinct peaks at 711.3 and 724.9 eV, assigned to the $2p_{3/2}$ and $2p_{1/2}$ orbitals of Fe^{2+}, respectively. The energy difference between these two peaks (ΔE = 13.6 eV) is consistent with the spin-orbit splitting energy of Fe^{2+}. In addition, peaks corresponding to the $2p_{3/2}$ and $2p_{1/2}$ orbitals of Fe^{3+} appear at 715.0 and 728.8 eV, which may result from the partial oxidation of Fe^{2+} during synthesis. In the Ca 2p spectrum, the $2p_{3/2}$ and $2p_{1/2}$ peaks of Ca^{2+} are located at 347.9

23669608, 0, Downloaded from https://onlinelibrary.wiley.com/doi/10.1002/smtd.70703 by Hu linfeng - Southeast University , Wiley Online Library on [11/05/2026]. See the Terms and Conditions (https://onlinelibrary.wiley.com/terms-and-conditions) on Wiley Online Library for rules of use; OA articles are governed by the applicable Creative Commons License

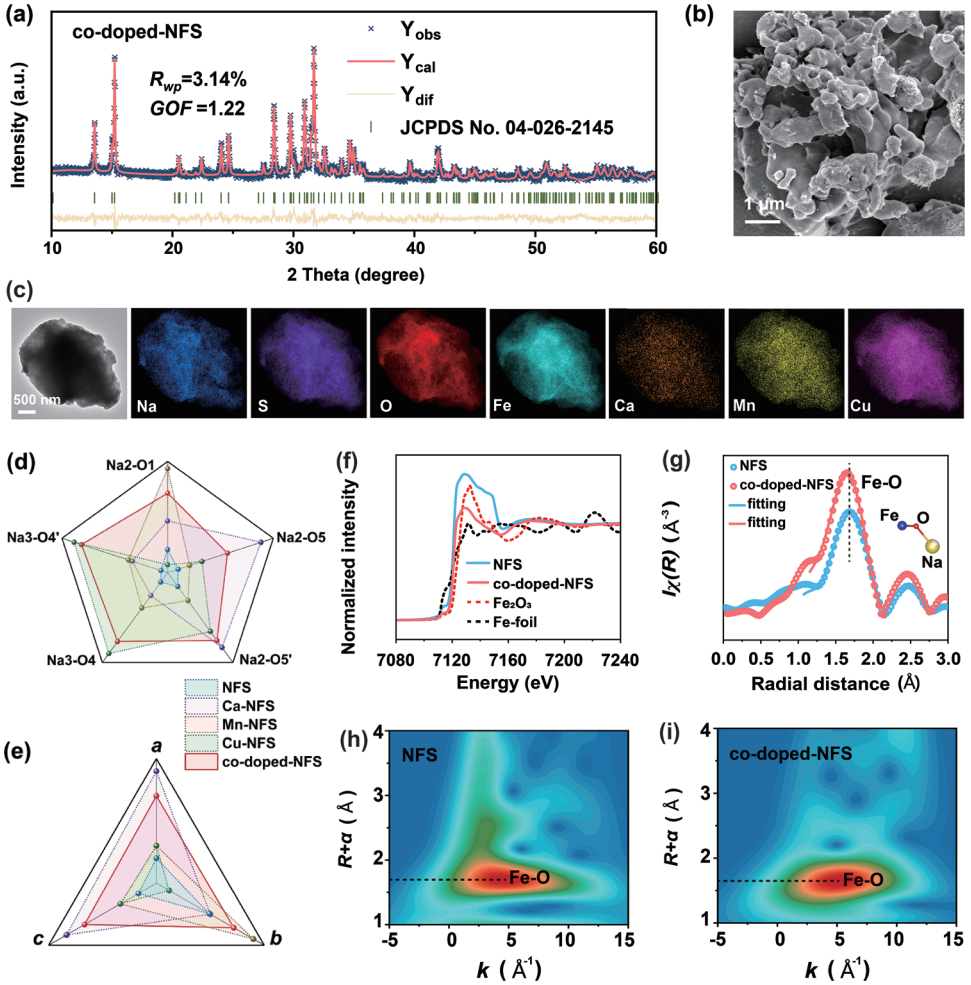

FIGURE 2 | (a) XRD Rietveld refinement profile of co-doped-NFS. The corresponding (b) SEM image. (c) TEM-EDS mappings. (d) Radar chart to show the Na—O bond length changes by Ca, Mn, Cu substitution. (e) Radar chart to show the corresponding lattice parameter evolution. (f) Fe *K*-edge XANES spectra. (g) Experimental Fe *K*-edge *R*-space EXAFS spectra and fitted curves for NFS and co-doped-NFS. Inset: Schematic of the bonding between Fe, O, and Na atoms. (h,i) Wavelet transform plots of pristine NFS and co-doped-NFS.

and 351.4 eV, respectively. For the Mn 2p spectrum, the $2p_{3/2}$ and $2p_{1/2}$ peaks of Mn^{2+} appear at 642.7 and 652.0 eV, with a satellite peak of Mn^{2+} observed at 647.2 eV. In the Cu 2p spectrum, the $2p_{3/2}$ and $2p_{1/2}$ peaks of Cu^{2+} are situated at 932.7 and 952.4 eV, respectively. These results confirm the successful doping of Ca^{2+}, Mn^{2+}, and Cu^{2+}. Additionally, elemental analysis by inductively coupled plasma atomic emission spectroscopy (ICP-AES, Figure S12). identifies that the actual atomic ratio of Fe: Ca: Mn: Cu in the co-doped sample was determined to be 19.69: 0.29: 0.37: 0.40, which is in good agreement with the designed stoichiometric ratio of 19.00: 0.30: 0.35: 0.35, corresponding to the target composition $Na_2Fe_{1.9}Ca_{0.03}Mn_{0.035}Cu_{0.035}(SO_4)_3$.

Subsequently, Rietveld refinement was performed on the PXRD data of the Ca, Mn, Cu co-doped sample to extract Na—O bond lengths and lattice parameters (Figure 2a,d,e, Table S6). As shown in Figure 2d,e, co-doping with Ca^{2+}, Mn^{2+} and Cu^{2+} results in synergistic elongation, simultaneously increasing Na—O bond lengths at both Na2 and Na3 sites as well as the *a*, *b*, *c* lattice parameters, as an overlapping effect of single doping [39–41]. Significantly, the bond length increments (Δ) for co-doped-NFS are $\Delta Na_2—O_1$ = 0.0071 Å, $\Delta Na_2—O_5$ = 0.0056 Å, $\Delta Na_2—O_5'$ = 0.0054 Å, $\Delta Na_3—O_4$ = 0.0119 Å, and $\Delta Na_3—O_4'$ = 0.0203 Å. Correspondingly, the lattice parameter expansions relative to NFS are Δa = 0.0050 Å, Δb = 0.0025 Å, and Δc = 0.0050 Å. Such a lattice expansion effectively widens the Na^+ migration channels along the *c*-axis in the $Na_2Fe_2(SO_4)_3$ crystal (Scheme 1b), thereby facilitating ion transport pathways that involve both Na_2 and Na_3 sites and weakening the electrostatic resistance encountered during Na^+ migration [42].

To further validate these structural evolution, synchrotron-based x-ray absorption fine structure (XAFS) measurements were conducted on both NFS and co-doped NFS samples. It is difficult to obtain Na K-edge x-ray absorption near edge structure (XANES) spectra due to its unsuitable energy. However, we can gain some Na—O bond information from the Fe—O bond evolution trend based on Fe K-edge absorption. As shown in Figure 2f, the binding energies of both the pristine NFS and co-doped NFS samples fall in the range between that of elemental Fe (7112.0 eV) and Fe_2O_3 (7120.0 eV), which is consistent with the characteristic binding energy of $Fe^{2+/3+}$. This finding is in good agreement with the $Fe^{2+/3+}$ valence state derived from XPS characterization. Compared with pristine NFS, the interatomic

23669608, 0, Downloaded from https://onlinelibrary.wiley.com/doi/10.1002/smtd.70703 by Hu linfeng - Southeast University , Wiley Online Library on [11/05/2026]. See the Terms and Conditions (https://onlinelibrary.wiley.com/terms-and-conditions) on Wiley Online Library for rules of use; OA articles are governed by the applicable Creative Commons License

distance between Fe and O in co-doped NFS decreases slightly (Figure 2g, Table S7), which is in agreement with the wavelet transformed extended x-ray absorption fine structure (EXAFS) results in Figure 2h,i. Consistently, the average Fe—O bond length was found to decrease by approximately 0.04 Å after co-doping in PXRD Rietveld refinement, which is fully agreement with the EXAFS measurements. Furthermore, the Fourier-transform infrared (FTIR) spectra (Figure S13) also show a shift of the S—O stretching mode to a higher wavenumber in co-doped-NFS (co-doped-NFS: 988.8 vs NFS: 987.4 cm^{-1}), suggest an increase on S—O bond energy. Combined with the aforementioned lattice volume expansion after co-doping, the shorted Fe—O and the increased S—O bond energy as evident by XAFS and FITR spectra further validate the successful elongation of Na2-O and Na3-O bonds in our alluaudite-typed $Na_2Fe_2(SO_4)_3$ [43].

2.3 | Greatly Enhancement on Sodium Ion Transport Kinetics

As mentioned above, the multi-cations co-doping strategy can elongate the Na—O bond lengths and lead to lattice expansion. To further validate the enhancement on the Na^+ transport ability of co-doped-NFS, galvanostatic intermittent titration technique (GITT) measurements were conducted to investigate the Na^+ diffusion kinetics during the charge and discharge processes. As shown in Figure 3a,b; Figures S14–S16, the Na^+ diffusion coefficients of co-doped-NFS (10^{-10} to 10^{-8} $cm^2 \cdot s^{-1}$) are significantly higher than those of NFS (10^{-11} to 10^{-9} $cm^2 \cdot s^{-1}$). This improvement by orders of magnitude indicates more efficient Na^+ intercalation and deintercalation kinetics within the co-doped-NFS framework, suggesting superior electrochemical performance. A comparison with previously reported data (Figure 3b) further confirms that the co-doped NFS electrode exhibits markedly enhanced Na^+ migration capability, offering distinct advantages for fast-charging and fast-discharging battery applications [19, 26, 44–49].

DFT calculations were performed to elucidate the Na^+ migration barriers and transport pathways after multi-cations doping. As shown in Figure 3c,d, DFT calculations of the migration barriers for Na^+ hopping between different sodium sites ($Na_1 \rightarrow Na_1$, $Na_2 \rightarrow Na_2$, see inset images in Figure 3c,d) revealed that the energy barriers in co-doped-NFS are consistently lower than those in NFS. Specifically, the $Na_2 \rightarrow Na_2$ migration barrier in co-doped-NFS is 0.33 eV, compared 0.38 eV in NFS. Similarly, the barrier for $Na_3 \rightarrow Na_3$ migration decreases from 0.34 eV in NFS to 0.30 eV in co-doped-NFS. More importantly, we further verified the widening of Na^+ migration channels via DFT calculations. Figure 3e reveals that the Na^+ transport pathways for Na2 and Na3 in co-doped-NFS are wider than those in NFS, thereby facilitating more continuous and favorable routes for Na^+ diffusion. These results conclusively demonstrates that the bond-tuning mechanism effectively broadens the Na^+ migration channels.

To further unravel the intrinsic mechanism by which the co-doping strategy enhances sodium storage kinetics, we performed DFT calculations to analyze the electronic structure and Na^+ adsorption behavior of the materials. As shown in Figure 3f, compared with the pristine NFS, the co-doped NFS exhibits a higher density of states near the Fermi level in the total density of states (TDOS), indicating that doping effectively enhances the metallic character of co-doped-NFS. The partial density of states (PDOS, Figure S17) results reveal that the density of states of Fe orbitals near the Fermi level is significantly enhanced after co-doping, and the contributions of the introduced Ca, Mn, and Cu orbitals further optimize the electronic structure. In addition, the Na^+ adsorption energy calculations (Figure 3g) show that the Na^+ adsorption energy of pristine NFS is −0.41 eV, while that of the ternary co-doped NFS is increased to −0.29 eV. Doping weakens the strong electrostatic interaction between Na^+ and the material surface, facilitating the rapid deintercalation and migration of Na^+. In summary, co-doped-NFS exhibits lower Na^+ migration barriers, broader migration channels, optimized electronic structure and reduced adsorption energy for Na^+ which collectively contribute to the enhanced Na^+ transport properties [19, 28, 50].

2.4 | Sodium-Ion Battery Performance

Half-cells employing NFS and co-doped-NFS cathodes were evaluated using cyclic voltammetry (CV) and galvanostatic charge-discharge (GCD) tests within a voltage range of 2.00–4.50 V. The initial cycled CV curve of co-doped-NFS sample exhibits three pairs of redox peaks (Figure S18). The sharp oxidation peak at 4.14 V (Peak 2) is attributed to Na^+ extraction from Na1 and Na2 sites, likely due to the high migration barriers of Na^+ at these sites. Correspondingly, the sharp reduction peak at 3.76 V (Peak 3) reflects Na^+ insertion into Na1 and Na2 sites. In contrast, the broad peaks at 3.69 V (Peak 1) and 3.42 V (Peak 4) are associated with desodiation/sodiation at the Na3 sites. During the oxidation process, Fe^{2+} is oxidized to Fe^{3+}, while the reduction process entails the conversion of Fe^{3+} back to Fe^{2+}. Simultaneously, variable scan rate CV tests were performed on co-doped-NFS samples with significantly reduced polarization. (Figure S19b) To further elucidate the enhanced Na^+ migration kinetics, electrochemical impedance spectroscopy (EIS) measurements were conducted. As shown in Figure S20, compared with the pristine NFS sample, the co-doped-NFS electrode exhibits not only a significantly reduced charge transfer resistance (R_{ct}), but also a distinctly increased diffusion slope corresponding to the Warburg impedance (W_o) in the low-frequency region. These findings confirm that the co-doping strategy effectively enhances the Na^+ diffusion kinetics and charge transfer capability of the material, which is consistent with the improved electrochemical performance observed in the CV and GITT tests.

The Na^+ intercalation/de-intercalation mechanism of our co-doped-NFS sample was confirmed by the ex situ XRD characterizations in a complete charge–discharge procedure, respectively (Figure S21). Noticeably, the co-doped-NFS sample delivers a discharge specific capacity of 97 $mAh \cdot g^{-1}$, much higher than the 83 $mAh \cdot g^{-1}$ of pristine NFS (Figure 4a), which may be attributed to the increased participation of Fe^{2+}/Fe^{3+} redox sites and enhanced electronic conductivity after co-doping. Corresponding to the distinct redox peaks observed in the CV curve for co-doped-NFS, two charge plateaus (around 4.10 and 3.70 V) and two discharge plateaus (around 3.80 and 3.40 V) are observed during the first cycle, which is well consistent with the interpretation of the CV results. Thus, the as-designed co-doped-NFS sample delivers a high energy density of 354.1 $Wh \cdot kg^{-1}$ owing

23669608, 0, Downloaded from https://onlinelibrary.wiley.com/doi/10.1002/smtd.70703 by Hu linfeng - Southeast University , Wiley Online Library on [11/05/2026]. See the Terms and Conditions (https://onlinelibrary.wiley.com/terms-and-conditions) on Wiley Online Library for rules of use; OA articles are governed by the applicable Creative Commons License

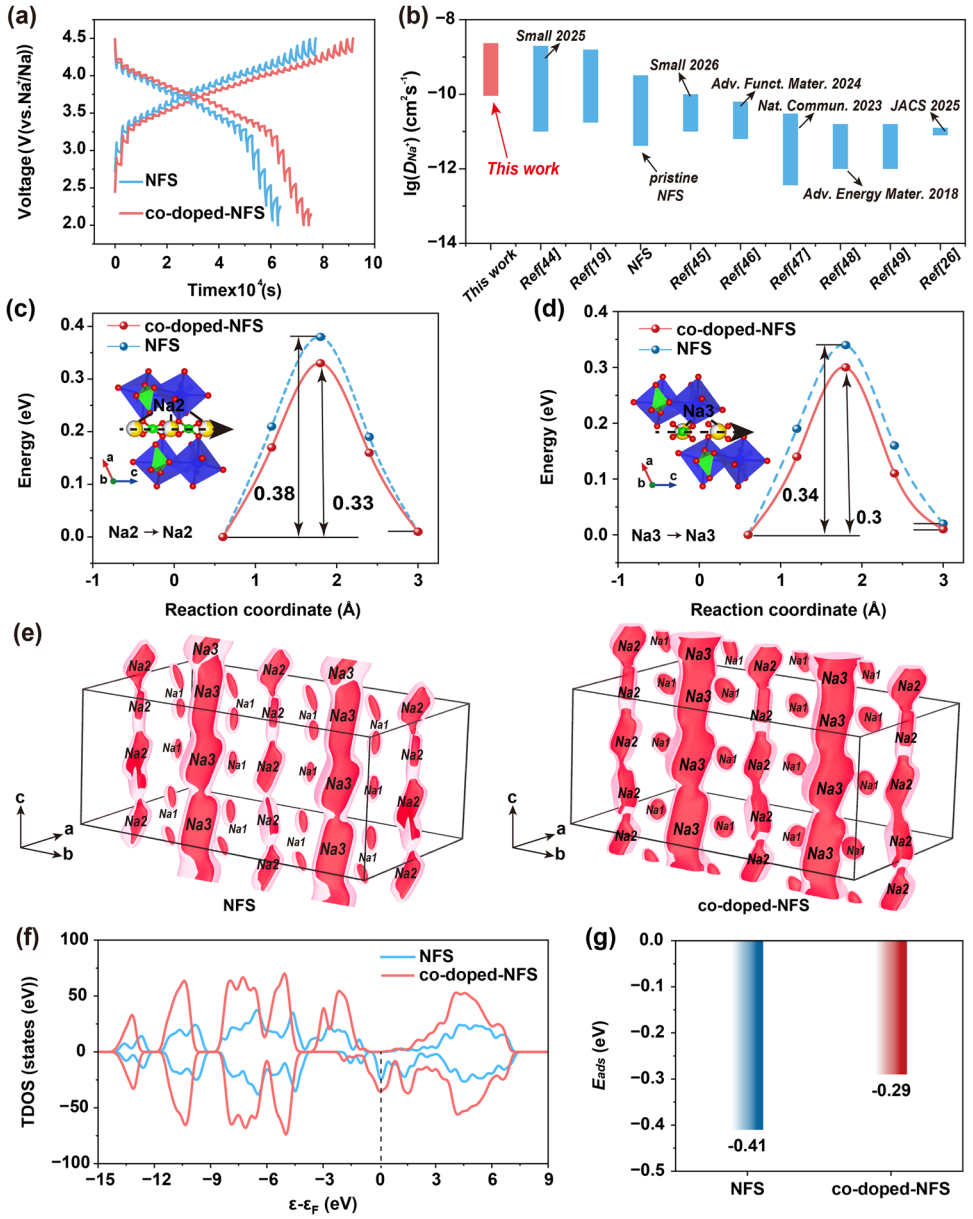

FIGURE 3 | (a) GITT profiles. (b) Comparison of Na^+ diffusion coefficients with values reported in literature. (c,d) Comparison of the Na^+ migration barriers between NFS and co-doped-NFS. Inset: Schematic illustration of Na^+ migration. (e) Comparison of Na^+ migration channels. (f) TDOS of NFS and co-doped-NFS. (g) Calculated E_{ads} for a Na^+ ion adsorbed of NFS and co-doped-NFS on the material surface.

to the enhanced capacity with well keeping the high operating voltage simultaneously. Note the as-achieved energy density of the co-doped-NFS sample exceeds most of the as-reported polyanionic cathode materials such as $Na_3V(PO_4)_2$ in SIBs (Figure 4b, Table S8) [51–65].

More importantly, benefited by the ultrafast Na^+ transport kinetics, the half-cell using the co-doped NFS cathode demonstrated excellent rate-performance and cycling stability. It delivers a reversible discharge specific capacities of 97, 80, and 69 mAh·g^{-1} at current densities of 0.1, 1.0, and 3.0 A·g^{-1}, respectively (Figure 4c; Figure S22). The excellent reversibility was confirmed by the capacity remaining at 94 mAh·g^{-1} when current density reduced to 0.1 A·g^{-1}. In contrast, NFS under the same conditions shows sequentially declining capacities of 83, 38, and 13 mAh·g^{-1}. The rate-capability of the co-doped NFS cathode at 3.0 A·g^{-1} is over five times higher than that of NFS (69 vs. 13 mAh·g^{-1}). Furthermore, Figure 4d,e and Figure S23, the co-doped-NFS exhibits outstanding cycling stability with a capacity retention rates of 67% after 5000 cycles at 3.0 A·g^{-1} and 85% after 600 cycles at 0.1 A·g^{-1}, respectively. Figure 4e shows a comparison of the lifespan obtained in our sample with other literature [66–73].

To further evaluate the practical applicability of the co-doped-NFS cathode material, a full cell was constructed by pairing it with hard carbon anode (Figure S24). This co-doped-NFS//hard carbon full cell exhibited a discharge plateau around 3.10 V and achieved a reversible specific capacity of about 80 mAh·g^{-1} at a current density of 0.1 A·g^{-1}, corresponding to a desirable energy density of 248.0 Wh·kg^{-1} based on the cathode mass loading of co-doped-NFS (Figure 4f). The full cell delivered reversible

23659608, 0, Downloaded from https://onlinelibrary.wiley.com/doi/10.1002/smtd.70703 by Hu linfeng - Southeast University , Wiley Online Library on [11/05/2026]. See the Terms and Conditions (https://onlinelibrary.wiley.com/terms-and-conditions) on Wiley Online Library for rules of use; OA articles are governed by the applicable Creative Commons License

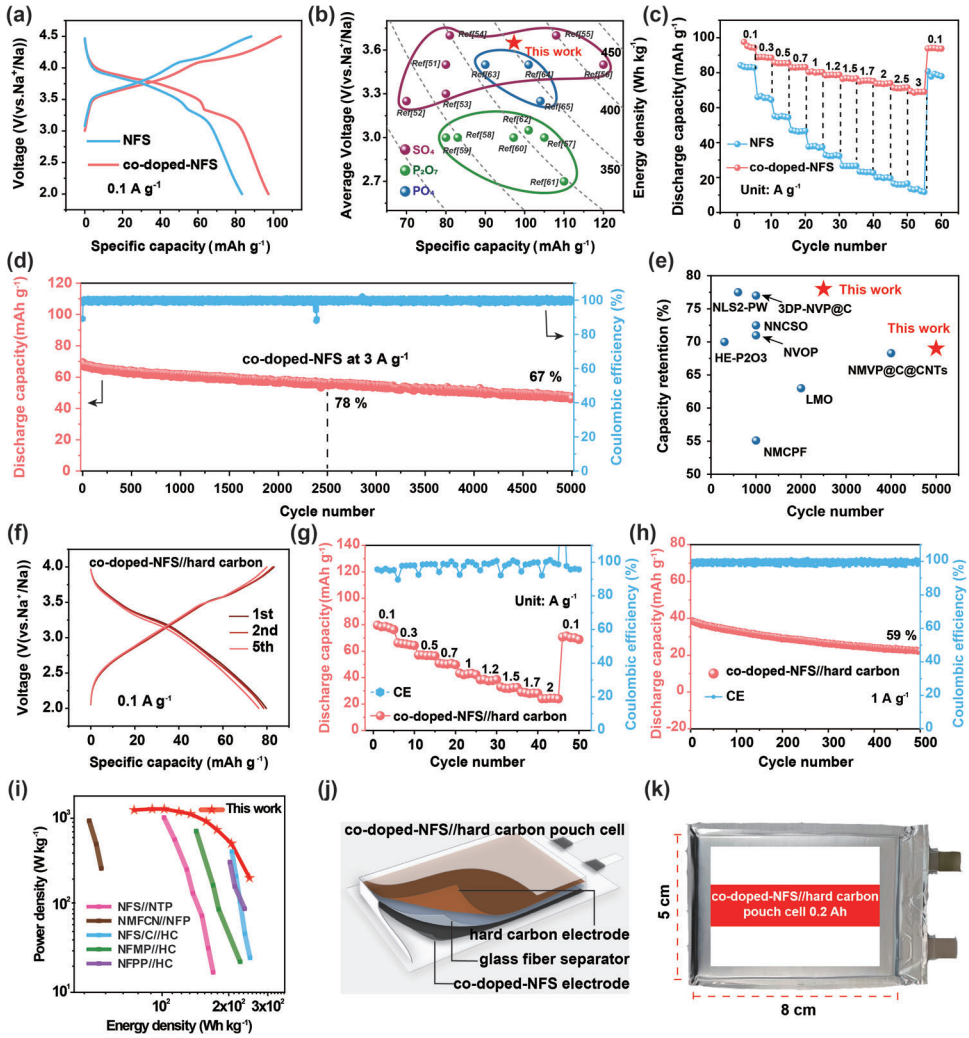

FIGURE 4 | (a) Charge/discharge profiles of NFS and co-doped-NFS at 0.1 A·g^{-1}. (b) Comparison of working voltage and specific discharge capacity among several polyanionic compounds. (c) Rate performance of half-cell. (d) Long-term cycling performance of half-cell. (e) Comparison of number of cycles and capacity retention with previously reported works. (f) Charge/discharge profiles of the co-doped-NFS//hard carbon coin full cell at 0.1 A·g^{-1}. (g) Rate performance of coin full cell. (h) Long-term cycling performance at 1.0 A·g^{-1} of coin full cell. (i) Ragone plots illustrating the energy density/power density comparison between full battery and other literature. (j) Schematic diagram of the co-doped-NFS//hard carbon pouch cell. (k) Digital photograph of the co-doped-NFS//hard carbon pouch cell.

capacities of 80, 66, 57, 51, 43, and 38 mAh·g^{-1} at current densities of 0.1, 0.3, 0.5, 0.7, 1.0, and 1.2 A·g^{-1}, respectively (Figure 4g). Even at a high current density of 1.0 A·g^{-1}, it retained about 54% of the capacity measured at 0.1 A·g^{-1}. Notably, when the current density was returned to 0.1 A·g^{-1}, the cell recovered a high capacity of ~70 mAh·g^{-1}, exhibiting excellent rate reversibility. In addition, long-term cycling stability was evaluated. 500 cyclability at 0.1 A·g^{-1} was confirmed of the full cell as shown in Figure 4h. Ragone plots in Figure 4i clearly display the advances of the sodium ion battery constructed from our co-doped-NFS cathode with the well balanced of energy density and power density compared to the other SIBs in the literature [46, 74–77]. Notably, the as-fabricated pouch cell delivers an energy density of approximately 190.8 Wh·kg^{-1} (based on the total mass of electroactive materials) and can successfully drive an LED indicator (Figure 4j,k; Figure S25), demonstrating its great potential for practical applications [78–80].

3 | Conclusion

In summary, we systematically investigated the effect of Ca, Mn, Cu, Mg, Al, Ti, V, Co, Ni, Zn single-element doping in $Na_2Fe_2(SO_4)_3$ and realized the synergetic elongation of Na_2—O/Na_3—O bonds in $Na_2Fe_2(SO_4)_3$ to widen the sodium ion transport channel by Ca, Mn, Cu co-doping. Specifically, Ca doping induced the elongation of the Na_2—O_5 and Na_2—O_5' bonds; Mn doping resulted in the pronounced extension of the Na_2—O_1 bond; and Cu doping led to the increase in the Na_3—O_4 and Na_3—O_4' bond lengths. The optimized $Na_2Fe_{1.9}Ca_{0.03}Mn_{0.035}Cu_{0.035}(SO_4)_3$ exhibits ultrafast sodium ion diffusion coefficient in the range of 10^{-10} to 10^{-8} cm^2·s^{-1}, which is the highest one among the $Na_2Fe_2(SO_4)_3$ cathode up to date. DFT calculations reveal that Ca, Mn, Cu co-doping in the alluaudite structure induces a considerable reduction in the Na^+ migration energy barrier and an enhancement in the

23669608, 0, Downloaded from https://onlinelibrary.wiley.com/doi/10.1002/smtd.70703 by Hu linfeng - Southeast University , Wiley Online Library on [11/05/2026]. See the Terms and Conditions (https://onlinelibrary.wiley.com/terms-and-conditions) on Wiley Online Library for rules of use; OA articles are governed by the applicable Creative Commons License

electronic density of states near the Fermi level. As a result, $Na_2Fe_2(SO_4)_3$ delivers a high energy density of 354.1 Wh·kg^{-1} at 0.1 A·g^{-1} and excellent rate capability (97, 80, and 69 mAh·g^{-1} at 0.1, 1.0, and 3.0 A·g^{-1}, respectively). It also demonstrates excellent cycling stability, retaining 69% of its capacity after 5000 cycles. The $Na_2Fe_{1.9}Ca_{0.03}Mn_{0.035}Cu_{0.035}(SO_4)_3$//hard carbon full-cell delivered a high energy density of 248.0 Wh·kg^{-1}. This study makes a breakthrough in the Na^+ transport kinetics bottleneck in $Na_2Fe_2(SO_4)_3$, and provides new insights on the structural evolution of Na_2—O/Na_3—O bonds by multiple metallic cations substitution of Fe-site.

Acknowledgements

This work was financially supported by the National Natural Science Foundation of China (Grant Nos. 52371214, 52171203), the Special Projects in Universities' Key Fields of Guangdong Province (Grant Nos. 2023ZDZX3008, 2025ZDZX3007), Guizhou Province Basic Research Program (Natural Sciences) Talent Team Support Project (QianKeHe-JiChuQNB [2025]003), Innovation Team for Advanced Electrochemical Energy Storage Devices and Key Materials of Guizhou Provincial Higher Education Institutions (QianJiaoJi [2023]054), Advanced Electrochemical Energy Storage Devices and Key Materials Technology Innovation Talent Team Construction of Guizhou Province (QKHPTRC-CXTD [2023]016).

Conflicts of Interest

The authors declare no conflicts of interest.

Data Availability Statement

The data that support the findings of this study are available from the corresponding author upon reasonable request.

References

1. C. Vaalma, D. Buchholz, M. Weil, and S. Passerini, "A Cost and Resource Analysis of Sodium-Ion Batteries," *Nature Reviews Materials* 3 (2018): 18013, http://10.1038/natrevmats.2018.13.

2. Y. Fang, L. Xiao, Z. Chen, X. Ai, Y. Cao, and H. Yang, "Recent Advances in Sodium-Ion Battery Materials," *Electrochemical Energy Reviews* 1 (2018): 294–323, http://10.1007/s41918-018-0008-x.

3. Q. Ni, Y. Bai, F. Wu, and C. Wu, "Polyanion-Type Electrode Materials for Sodium-Ion Batteries," *Advanced Science* 4 (2017): 1600275, http://10.1002/advs.201600275.

4. Z. Cui, C. Liu, and A. Manthiram, "A Perspective on Pathways Toward Commercial Sodium-Ion Batteries," *Advanced Materials* 37 (2025): 2420463, http://10.1002/adma.202420463.

5. T. Jin, H. Li, K. Zhu, P.-F. Wang, P. Liu, and L. Jiao, "Polyanion-Type Cathode Materials for Sodium-Ion Batteries," *Chemical Society Reviews* 49 (2020): 2342–2377, http://10.1039/c9cs00846b.

6. Q. Liu, Z. Hu, M. Chen, et al., "The Cathode Choice for Commercialization of Sodium-Ion Batteries: Layered Transition Metal Oxides versus Prussian Blue Analogs," *Advanced Functional Materials* 30 (2020): 1909530, http://10.1002/adfm.201909530.

7. M. Jiang, Y. Zhao, Z. Hou, et al., "Leveraging Sodium Storage of Water-Deficient Prussian Blue Analogues by Deep Eutectic Chemistry," *ACS Energy Letters* 11 (2025): 526–536, http://10.1021/acsenergylett.5c03085.

8. M. Jiang, T. Li, X. Wei, et al., "Resolving Water-Induced Deactivity and Fragility of Prussian Blue by Eutectic Chemistry for Upgraded Sodium Storage," *Journal of Energy Chemistry* 118 (2026): 169–177, http://10.1016/j.jechem.2026.03.024.

9. N. Yabuuchi, M. Kajiyama, J. Iwatate, et al., "P2-Type $Na_x[Fe_{1/2}Mn_{1/2}]O_2$ Made From Earth-Abundant Elements for Rechargeable Na Batteries," *Nature Materials* 11 (2012): 512–517, http://10.1038/nmat3309.

10. B. Peng, Z. Zhou, J. Shi, X. Huang, Y. Li, and L. Ma, "Earth-Abundant Fe-Mn-Based Compound Cathodes for Sodium-Ion Batteries: Challenges and Progress," *Advanced Functional Materials* 34 (2024): 2311816, http://10.1002/adfm.202311816.

11. Y. Gao, H. Zhang, X.-H. Liu, et al., "Low-Cost Polyanion-Type Sulfate Cathode for Sodium-Ion Battery," *Advanced Energy Materials* 11 (2021): 2101751, http://10.1002/aenm.202101751.

12. P. Barpanda, G. Oyama, S. Nishimura, S. C. Chung, and A. Yamada, "A 3.8-V Earth-Abundant Sodium Battery Electrode," *Nature Communications* 5 (2014): 4358, http://10.1038/ncomms5358.

13. G. Oyama, S. Nishimura, Y. Suzuki, M. Okubo, and A. Yamada, "Off-Stoichiometry in Alluaudite-Type Sodium Iron Sulfate Na_{2+2x} $Fe_{2-x}(SO_4)_3$ as an Advanced Sodium Battery Cathode Material," *ChemElectroChem* 2 (2015): 1019–1023, http://10.1002/celc.201500036.

14. G. Oyama, O. Pecher, K. J. Griffith, et al., "Sodium Intercalation Mechanism of 3.8 V Class Alluaudite Sodium Iron Sulfate," *Chemistry of Materials* 28 (2016): 5321–5328, http://10.1021/acs.chemmater.6b01091.

15. P. Barman, D. Dwibedi, K. Jayanthi, et al., "Aqueous Spray-Drying Synthesis of Alluaudite $Na_{2+2x}Fe_{2-x}(SO_4)_3$ Sodium Insertion Material: Studies of Electrochemical Activity, Thermodynamic Stability, and Humidity-Induced Phase Transition," *Journal of Solid State Electrochemistry* 26 (2022): 1941–1950, http://10.1007/s10008-022-05142-w.

16. S.-I. Nishimura, Y. Suzuki, J. Lu, S. Torii, T. Kamiyama, and A. Yamada, "High-Temperature Neutron and X-ray Diffraction Study of Fast Sodium Transport in Alluaudite-type Sodium Iron Sulfate," *Chemistry of Materials* 28 (2016): 2393–2399, http://10.1021/acs.chemmater.6b00604.

17. P. Barpanda, "Pursuit of Sustainable Iron-Based Sodium Battery Cathodes: Two Case Studies," *Chemistry of Materials* 28 (2016): 1006–1011, http://10.1021/acs.chemmater.5b03926.

18. T. Jungers, A. Mahmoud, C. Malherbe, F. Boschini, and B. Vertruyen, "Sodium Iron Sulfate Alluaudite Solid Solution for Na-Ion Batteries: Moving Towards Stoichiometric $Na_2Fe_2(SO_4)_3$," *Journal of Materials Chemistry A* 7 (2019): 8226–8233, http://10.1039/c9ta00116f.

19. L. Wen, J. Zhang, J. Zhang, et al., "Cation-Inspired Polyhedral Distortion Boosting Moisture/Electrolyte Stability of Iron Sulfate Cathode for Durable High-Temperature Sodium-Ion Storage," *eScience* 5 (2025): 100313, http://10.1016/j.esci.2024.100313.

20. Y. Liu, R. Rajagopalan, E. Wang, et al., "Insight Into the Multirole of Graphene in Preparation of High Performance $Na_{2+2x}Fe_{2-x}(SO_4)_3$ Cathodes," *ACS Sustainable Chemistry & Engineering* 6 (2018): 16105–16112, http://10.1021/acssuschemeng.8b02679.

21. J. Wu, W. Zhou, S. Zhang, et al., "A Synergistic Cu/Ca Dual-Doping Strategy for High-Stability and Fast-Charging O_3-Type Cathode in Sodium-Ion Batteries," *Angewandte Chemie International Edition* 64 (2025): 202519551, http://10.1002/anie.202519551.

22. J. Lin, X. Shi, J. Xu, L. Shao, and Z. Sun, "Enabling Accelerated Na^+ Dynamics Through Li-Induced Electrostatic Shielding for High-Performance Na_3 $V_2(PO_4)_2F_3$ Cathode," *Advanced Energy Materials* 15 (2025): 2501979, http://10.1002/aenm.202501979.

23. Z.-Y. Li, H. Wang, W. Yang, et al., "Modulating the Electrochemical Performances of Layered Cathode Materials for Sodium Ion Batteries Through Tuning Coulombic Repulsion Between Negatively Charged TMO_2 Slabs," *ACS Applied Materials & Interfaces* 10 (2018): 1707–1718, http://10.1021/acsami.7b15590.

24. J. Wang, Y. Yang, J. Chen, et al., "Advanced Fast-Charging Anode Designs for Sodium-Ion Batteries," *Progress in Materials Science* 156 (2026): 101564, http://10.1016/j.pmatsci.2025.101564.

23669608, 0, Downloaded from https://onlinelibrary.wiley.com/doi/10.1002/smtd.70703 by Hu linfeng - Southeast University , Wiley Online Library on [11/05/2026]. See the Terms and Conditions (https://onlinelibrary.wiley.com/terms-and-conditions) on Wiley Online Library for rules of use; OA articles are governed by the applicable Creative Commons License

25. C. Xu, Q. Fu, W. Hua, et al., "Overcoming Kinetic Limitations of Polyanionic Cathode Toward High-Performance Na-Ion Batteries," *ACS Nano* 18 (2024): 18758–18768, http://10.1021/acsnano.4c06510.

26. C. Liu, K. Chen, F. Li, et al., "Unlocking Phase Purity of Sodium Iron Sulfate for Low-Cost and High-Performance Sodium-Ion Batteries," *Journal of the American Chemical Society* 147 (2025): 14635–14646, http://10.1021/jacs.5c02485.

27. A. Zhao, F. Ji, C. Liu, et al., "Revealing the structural chemistry in $Na_{6-2x}Fe_x$ $(SO_4)_3$ $(1.5 \leq x \leq 2.0)$ for low-cost and high-performance sodium-ion batteries," *Science Bulletin* 68 (2023): 1894–1903, http://10.1016/j.scib.2023.07.034.

28. Q. Zhou, Y. Xin, Y. Wang, et al., "Electronic Structure Engineering Through Strengthened d–p Orbital Hybridization of Sodium Ferric Sulfate Cathode With Enhanced Electrochemical Performance for Sodium-Ion Batteries," *Energy Storage Materials* 76 (2025): 104138, http://10.1016/j.ensm.2025.104138.

29. Z. Wu, C. Lu, F. Ye, et al., "Bilayered $VOPO_4 \cdot 2H_2O$ Nanosheets With High-Concentration Oxygen Vacancies for High-Performance Aqueous Zinc-Ion Batteries," *Advanced Functional Materials* 31 (2021): 2106816, http://10.1002/adfm.202106816.

30. Z. Wu, F. Ye, Q. Liu, et al., "Simultaneous Incorporation of V and Mn Element Into Polyanionic NASICON for High Energy-Density and Long-Lifespan Zn-Ion Storage," *Advanced Energy Materials* 12 (2022): 2200654, http://10.1002/aenm.202200654.

31. F. Ye, R. Pang, C. Lu, et al., "Reversible Ammonium Ion Intercalation/de-intercalation With Crystal Water Promotion Effect in Layered $VOPO_4 \cdot 2H_2$ O**," *Angewandte Chemie International Edition* 62 (2023): 202303480, http://10.1002/anie.202303480.

32. L. L. Wong, H. M. Chen, and S. Adams, "Sodium-Ion Diffusion Mechanisms in the Low Cost High Voltage Cathode Material $Na_{2+\delta}Fe_{2-\delta/2}(SO_4)_3$," *Physical Chemistry Chemical Physics* 17 (2015): 9186–9193, http://10.1039/c5cp00380f.

33. A. Plewa, A. Kulka, E. Hanc, et al., "Facile Aqueous Synthesis of High Performance $Na_2FeM(SO_4)_3$ (M = Fe, Mn, Ni) Alluaudites for Low Cost Na-Ion Batteries," *Journal of Materials Chemistry A* 8 (2020): 2728–2740, http://10.1039/c9ta11565j.

34. Z. Wang, H. Chen, Q. Zhao, et al., "High Entropy Induced Lattice Expansion in Layered Oxide Cathode Towards Fast Sodium Storage," *Energy Storage Materials* 71 (2024): 103617, http://10.1016/j.ensm.2024.103617.

35. Y. Q. Ye, S. H. Liu, W. Q. Lv, et al., "Mn-Doped-Iron Sulfide as Long-Term Stability Anode for High-Performance Sodium-Ion Batteries at Wide Temperature and High-Rate Conditions," *Advanced Functional Materials* 36 (2025): 19847, http://10.1002/adfm.202519847.

36. D. Xie, Y. Wang, L. Tian, et al., "Dual-Functional Ca-Ion-Doped Layered δ-MnO_2 Cathode for High-Performance Aqueous Zinc-Ion Batteries," *Advanced Functional Materials* 35 (2024): 2413993, http://10.1002/adfm.202413993.

37. Y. Xin, Y. Wang, Q. Zhou, et al., "The Importance of Bond Covalency for the Activation of Multielectron Reactions in Phosphate Cathodes for Sodium-Ion Batteries," *Energy Storage Materials* 72 (2024): 103770, http://10.1016/j.ensm.2024.103770.

38. P.-F. Wang, Y. Xiao, N. Piao, et al., "Both Cationic and Anionic Redox Chemistry in A P2-Type Sodium Layered Oxide," *Nano Energy* 69 (2020): 104474, http://10.1016/j.nanoen.2020.104474.

39. W. Zheng, G. Liang, Q. Liu, et al., "The Promise of High-Entropy Materials for High-Performance Rechargeable Li-Ion and Na-Ion Batteries," *Joule* 7 (2023): 2732–2748, http://10.1016/j.joule.2023.10.016.

40. Z. Zhou, Y. Ma, T. Brezesinski, B. Breitung, Y. Wu, and Y. Ma, "Improving Upon Rechargeable Battery Technologies: On the Role of High-Entropy Effects," *Energy & Environmental Science* 18 (2025): 19–52, http://10.1039/d4ee03708a.

41. K. Du, Y. Liu, Y. Yang, et al., "High Entropy Oxides Modulate Atomic-Level Interactions for High-Performance Aqueous Zinc-Ion Batteries," *Advanced Materials* 35 (2023): 2301538, http://10.1002/adma.202301538.

42. C. Cheng, D. Wu, T. Gong, et al., "Internal and External Cultivation Design of Zero-Strain Columbite-Structured MNb_2O_6 Toward Lithium-Ion Capacitors as Competitive Anodes," *Advanced Energy Materials* 13 (2023): 2302107, http://10.1002/aenm.202302107.

43. W. Zeng, F. Xia, J. Wang, et al., "Entropy-Increased $LiMn_2O_4$-Based Positive Electrodes for Fast-Charging Lithium Metal Batteries," *Nature Communications* 15 (2024): 7371, http://10.1038/s41467-024-51168-1.

44. S. D. Pinjari, P. Mudavath, R. C. Dutta, et al., "Single-Phase Solid-Solution Reaction Facilitated Sodium-Ion Storage in Indium-Substituted Monoclinic Sodium-Iron Phosphomolybdate Cathodes," *Small* 21 (2025): 2501004, http://10.1002/smll.202501004.

45. A. Phukan, B. Patra, T. Acharya, et al., "Realizing Highly Reversible Nb^{5+} /Nb^{4+} /Nb^{3+} Redox Reactions in Bulk NASICON-$NaNbAl(PO_4)_3$ Anode Under Higher Current Rates," *Small* 22 (2026): 10012, http://10.1002/smll.202510012.

46. S. Zhao, G. Li, Z. Li, et al., "Fast Charging Sodium-Ion Full Cell Operated From −50°C to 90°C," *Advanced Functional Materials* 35 (2024): 2411007, http://10.1002/adfm.202411007.

47. J. Zhang, Y. Yan, X. Wang, et al., "Bridging Multiscale Interfaces for Developing Ionically Conductive High-Voltage Iron Sulfate-Containing Sodium-Based Battery Positive Electrodes," *Nature Communications* 14 (2023): 3701, http://10.1038/s41467-023-39384-7.

48. M. Chen, D. Cortie, Z. Hu, et al., "A Novel Graphene Oxide Wrapped $Na_2Fe_2(SO_4)_3$/C Cathode Composite for Long Life and High Energy Density Sodium-Ion Batteries," *Advanced Energy Materials* 8 (2018): 1800944, http://10.1002/aenm.201800944.

49. S. Li, W. Wang, Y. Jia, et al., "Colloidal Synthesis of $Na_2Fe_2(SO_4)_3$ Nanocrystals as the Cathode Toward High-Rate Capability and High-Energy Density Sodium-ion Batteries," *Small Methods* 9 (2025): 2402110, http://10.1002/smtd.202402110.

50. Y. Li, Q. Xiao, Y. Zhao, S. Zhao, and B. Liu, "Mg-Doped Single-Crystalline $Na_{2+2x}Fe_{2-x}(SO_4)_3$ Cathode Materials With Greatly Improved Rate Performance and Stable Cyclability for Low-Cost Na-Ion Batteries," *Energy Storage Materials* 80 (2025): 104408, http://10.1016/j.ensm.2025.104408.

51. D. Dwibedi, C. D. Ling, R. B. Araujo, et al., "Ionothermal Synthesis of High-Voltage Alluaudite $Na_{2+2x}Fe_{2-x}(SO_4)_3$ Sodium Insertion Compound: Structural, Electronic, and Magnetic Insights," *ACS Applied Materials & Interfaces* 8 (2016): 6982–6991, http://10.1021/acsami.5b11302.

52. P. Barpanda, G. Oyama, C. D. Ling, and A. Yamada, "Kröhnkite-Type $Na_2Fe(SO_4)_2 \cdot 2H_2O$ as a Novel 3.25 V Insertion Compound for Na-Ion Batteries," *Chemistry of Materials* 26 (2014): 1297–1299, http://10.1021/cm4033226.

53. P. Singh, K. Shiva, H. Celio, and J. B. Goodenough, "Eldfellite, $NaFe(SO_4)_2$: An Intercalation Cathode Host for Low-Cost Na-Ion Batteries," *Energy & Environmental Science* 8 (2015): 3000–3005, http://10.1039/c5ee02274f.

54. W. Pan, W. Guan, S. Liu, et al., "$Na_2Fe(SO_4)_2$: An Anhydrous 3.6 V, Low-Cost and Good-Safety Cathode for a Rechargeable Sodium-Ion Battery," *Journal of Materials Chemistry A* 7 (2019): 13197–13204, http://10.1039/c9ta02188d.

55. W. Yang, Q. Liu, Q. Yang, et al., "Dendritic Conductive Carbon Networks Enhance Na^+ Transport in $Na_{2+2\delta}Fe_{2-\delta}(SO_4)_3$@C Cathode for Fast Charging and Wide Temperature Sodium-Ion Batteries," *Nano Energy* 141 (2025): 111075, http://10.1016/j.nanoen.2025.111075.

56. Y. Zhao, F. Wu, M. Jiang, et al., "Yolk-Shell Sodium Iron Sulfate@Carbon for Advanced Sodium Storage With Enhanced Capacity and Stability," *Small* 21 (2025): 2506866, http://10.1002/smll.202506866.

23669608, 0, Downloaded from https://onlinelibrary.wiley.com/doi/10.1002/smtd.70703 by Hu linfeng - Southeast University , Wiley Online Library on [11/05/2026]. See the Terms and Conditions (https://onlinelibrary.wiley.com/terms-and-conditions) on Wiley Online Library for rules of use; OA articles are governed by the applicable Creative Commons License

57. M. Chen, L. Chen, Z. Hu, et al., "Carbon-Coated $Na_{3.32}Fe_{2.34}(P_2O_7)_2$ Cathode Material for High-Rate and Long-Life Sodium-Ion Batteries," *Advanced Materials* 29 (2017): 1605535, http://10.1002/adma.201605535.

58. P. Barpanda, G. Liu, C. D. Ling, et al., "$Na_2FeP_2O_7$: A Safe Cathode for Rechargeable Sodium-ion Batteries," *Chemistry of Materials* 25 (2013): 3480–3487, http://10.1021/cm401657c.

59. P. Barpanda, J. Lu, T. Ye, et al., "A Layer-Structured $Na_2CoP_2O_7$ Pyrophosphate Cathode for Sodium-Ion Batteries," *RSC Advances* 3 (2013): 3857–3860, http://10.1039/c3ra23026k.

60. H. J. Song, D.-S. Kim, J.-C. Kim, S.-H. Hong, and D.-W. Kim, "An Approach to Flexible Na-Ion Batteries With Exceptional Rate Capability and Long Lifespan Using $Na_2FeP_2O_7$ Nanoparticles On Porous Carbon Cloth," *Journal of Materials Chemistry A* 5 (2017): 5502–5510, http://10.1039/c7ta00727b.

61. B. Lin, S. Zhang, and C. Deng, "Understanding the Effect of Depressing Surface Moisture Sensitivity on Promoting Sodium Intercalation in Coral-Like $Na_{3.12}Fe_{2.44}(P_2O_7)_2$ /C Synthesized via a Flash-Combustion Strategy.4$(P_2O_7)_2$/C Synthesized via A Flash-Combustion Strategy," *Journal of Materials Chemistry A* 4 (2016): 2550–2559, http://10.1039/c5ta09403h.

62. Y. Niu, M. Xu, C. Cheng, et al., "$Na_{3.12}Fe_{2.3}(P_2Na_{3.12}Fe_{2.44}$ $(P_2O_7)_2$ /Multi-Walled Carbon Nanotube Composite as a Cathode Material for Sodium-Ion Batteries," *Journal of Materials Chemistry A* 3 (2015): 17224–17229, http://10.1039/c5ta03127c.

63. J. Kim, G. Yoon, H. Kim, Y.-U. Park, and K. Kang, "$Na_3V(PO_4)_2$: A New Layered-Type Cathode Material With High Water Stability and Power Capability for Na-Ion Batteries," *Chemistry of Materials* 30 (2018): 3683–3689, http://10.1021/acs.chemmater.8b00458.

64. W. Zhou, L. Xue, X. Lü, et al., "Na$xMV(PO_4)_3$ (M = Mn, Fe, Ni) Structure and Properties for Sodium Extraction," *Nano Letters* 16 (2016): 7836–7841, http://10.1021/acs.nanolett.6b04044.

65. F. Xiong, J. Li, C. Zuo, et al., "Mg-Doped $Na_4Fe_3(PO_4)_2(P_2O_7)$/C Composite With Enhanced Intercalation Pseudocapacitance for Ultra-Stable and High-Rate Sodium-Ion Storage," *Advanced Functional Materials* 33 (2022): 2211257, http://10.1002/adfm.202211257.

66. R. Li, X. Qin, X. Li, et al., "High-Entropy and Multiphase Cathode Materials for Sodium-Ion Batteries," *Advanced Energy Materials* 14 (2024): 2400127, http://10.1002/aenm.202400127.

67. K.-R. Ren, L. Chen, C.-Z. Liu, et al., "Ligand Field Electronic State Regulation of Monoclinic Prussian White Toward Highly Stable Sodium-Ion Batteries," *Advanced Materials* 37 (2025): 2507960, http://10.1002/adma.202507960.

68. N. Voronina, H. J. Kim, A. Konarov, et al., "Electronic Structure Engineering of Honeycomb Layered Cathode Material for Sodium-Ion Batteries," *Advanced Energy Materials* 11 (2021): 2003399, http://10.1002/aenm.202003399.

69. W. Zhang, Z. Zhang, H. Li, et al., "Engineering 3D Well-Interconnected Na4MnV(PO4)3 Facilitates Ultrafast and Ultrastable Sodium Storage," *ACS Applied Materials & Interfaces* 11 (2019): 35746–35754, http://10.1021/acsami.9b12214.

70. W. Zhang, Y. Wu, Y. Dai, et al., ""Mn-Locking" Effect by Anionic Coordination Manipulation Stabilizing Mn-Rich Phosphate Cathodes," *Chemical Science* 14 (2023): 8662–8671, http://10.1039/d3sc03095d.

71. H. Xiong, R. Qian, Z. Liu, et al., "A Polymer-Assisted Spinodal Decomposition Strategy Toward Interconnected Porous Sodium Super Ionic Conductor-Structured Polyanion-Type Materials and Their Application as a High-Power Sodium-Ion Battery Cathode," *Advanced Science* 8 (2021): 2004943, http://10.1002/advs.202004943.

72. J. Li, Y. Qi, F. Xiao, S. Bao, and M. Xu, "A Facilely-Synthesized Polyanionic Cathode With Impressive Long-Term Cycling Stability for Sodium-Ion Batteries," *Chemical Communications* 57 (2021): 9566–9569, http://10.1039/d1cc02203b.

73. S. Lee, Y. Cho, H. K. Song, K. T. Lee, and J. Cho, "Carbon-Coated Single-Crystal $LiMn_2O_4$ Nanoparticle Clusters as Cathode Material for High-Energy and High-Power Lithium-Ion Batteries," *Angewandte Chemie International Edition* 51 (2012): 8748–8752, http://10.1002/anie.201203581.

74. S. Qiu, X. Wu, M. Wang, et al., "NASICON-Type $Na_3Fe_2(PO_4)_3$ as a Low-Cost and High-Rate Anode Material for Aqueous Sodium-Ion Batteries," *Nano Energy* 64 (2019): 103941, http://10.1016/j.nanoen.2019.103941.

75. W. Yang, Q. Liu, Q. Yang, et al., "Transitioning From Anhydrous Stanfieldite-Type $Na_2Fe(SO_4)_2$ Precursor to Alluaudite-type $Na_{2+2\delta}Fe_{2-\delta}(SO_4)_3$/C Composite Cathode: A Pathway to Cost-Effective and All-Climate Sodium-Ion Batteries," *Energy Storage Materials* 74 (2025): 103925, http://10.1016/j.ensm.2024.103925.

76. H. Wang, J. An, W. Zhao, et al., "Constructing Heterotransition Metal Ligand Field Clusters With a Compact Spatial Structure for Maintaining Unimpeded Sodium-Ion Migration," *ACS Nano* 19 (2025): 34966–34980, http://10.1021/acsnano.5c11413.

77. X. Hu, S. Liang, J. Lin, et al., "Synergistic Configurational Entropy and Iron Vacancy Engineering in $Na_4Fe_3(PO_4)_2P_2O_7$ Cathode for High-Power-Density and Ultralong-Life Na-Ion Full Batteries," *Advanced Energy Materials* 15 (2024): 2404965, http://10.1002/aenm.202404965.

78. Z. He, T. Han, W. Liu, et al., "3D Printed Sodium-Ion Batteries via Ternary Anode Design Affording Hybrid Ion Storage Mechanism," *Advanced Energy Materials* 14 (2024): 2303296, http://10.1002/aenm.202303296.

79. T. Han, Z. He, W. Kuang, J. Zhou, and Y. Li, "3D Printing of Porous Hollow Nanosphere MoS_2@NiS/rGO Scaffolds Empowering Long-Cycle Sodium-Ion Batteries," *Nano Energy* 128 (2024): 109953, http://10.1016/j.nanoen.2024.109953.

80. T. Han, Z. Cui, W. Kuang, Y. Cai, J. Sun, and Y. Li, "Ferroelectric Nanofiber Reinforced Electrolyte Empowers Fully 3D-Printed Solid-State Sodium-Ion Batteries," *Advanced Functional Materials* 36 (2025): 202513625, http://10.1002/adfm.202513625.

Supporting Information

Additional supporting information can be found online in the Supporting Information section.

Supporting File: smtd70703-sup-0001-SuppMat.docx.

23669608, 0, Downloaded from https://onlinelibrary.wiley.com/doi/10.1002/smtd.70703 by Hu linfeng - Southeast University , Wiley Online Library on [11/05/2026]. See the Terms and Conditions (https://onlinelibrary.wiley.com/terms-and-conditions) on Wiley Online Library for rules of use; OA articles are governed by the applicable Creative Commons License